

Ultrashort highly localized wavepackets

M. Bock, S. K. Das, and R. Grunwald*

Max Born Institute for Nonlinear Optics and Short-Pulse Spectroscopy, Max-Born-Strasse 2a, D-12489 Berlin, Germany

*grunwald@mbi-berlin.de

Abstract: The recently introduced concept of radially non-oscillating, temporally stable ultrashort-pulsed Bessel-like beams we referred to as needle beams is generalized to a particular class of highly localized wavepackets (HLWs). Spatio-temporally quasi-nondiffracting pulses propagating along extended zones are shaped from Ti:sapphire oscillator radiation with a spatial light modulator and characterized with spatially resolved second order autocorrelation. Few-cycle wavepackets tailored to resemble circular disks, rings and bars of light represent the closest approximation of linear-optical light bullets known so far. By combining multiple HLWs, complex pulsed nondiffracting patterns are obtained.

©2012 Optical Society of America

OCIS codes: (320.0320) Ultrafast optics; (320.5540) Pulse shaping.

References and links

1. P. Saari, "How small a packet of photons can be made?" *Laser Phys.* **16**(4), 556–561 (2006).
2. P. Saari, "Photon Localization Revisited," in: *Quantum Optics and Laser Experiments* Sergiy Lyagushin Ed. (InTech - Open Access Publisher, Croatia, 2012), 49–66.
3. P. Saari, M. Menert, and H. Valtna, "Photon localization barrier can be overcome," *Opt. Commun.* **246**(4-6), 445–450 (2005).
4. B. Piglosiewicz, D. Sadiq, M. Mascheck, S. Schmidt, M. Silies, P. Vasa, and C. Lienau, "Ultrasmall bullets of light-focusing few-cycle light pulses to the diffraction limit," *Opt. Express* **19**(15), 14451–14463 (2011).
5. S. Trillo and W. Torruellas Eds, *Spatial Solitons* (Springer, Berlin, 2001), pp. 73–74.
6. Y. S. Kivshar and G. P. Agrawal, *Optical solitons - From fibers to photonic crystals* (Academic Press, Elsevier Science, Amsterdam, 2003), pp. 226–228.
7. H. Sönajal, M. Rätsep, and P. Saari, "Demonstration of the Bessel-X pulse propagating with strong lateral and longitudinal localization in a dispersive medium," *Opt. Lett.* **22**(5), 310–312 (1997).
8. P. Di Trapani, G. Valiulis, A. Piskarskas, O. Jedrkiewicz, J. Trull, C. Conti, and S. Trillo, "Spontaneously generated X-shaped light bullets," *Phys. Rev. Lett.* **91**(9), 093904 (2003).
9. P. T. Rakich, M. S. Dahlem, S. Tandon, M. Ibanescu, M. Soljacić, G. S. Petrich, J. D. Joannopoulos, L. A. Kolodziejski, and E. P. Ippen, "Achieving centimetre-scale supercollimation in a large-area two-dimensional photonic crystal," *Nat. Mater.* **5**(2), 93–96 (2006).
10. J. A. Stratton, *Electromagnetic Theory* (McGraw Hill, New York, 1941), 356.
11. J. Durmin, "Exact solution for nondiffracting beams I - The scalar theory," *J. Opt. Soc. Am. A* **4**(4), 651–654 (1987).
12. J. Durmin, J. J. Miceli, Jr., and J. H. Eberly, "Diffraction-free beams," *Phys. Rev. Lett.* **58**(15), 1499–1501 (1987).
13. H. E. Hernández-Figueroa, M. Zamboni-Rached, and E. Recami, eds., *Localized Waves, Theory and Experiments* (Wiley & Sons, New York, 2008).
14. Z. Bouchal, J. Wagner, and M. Chlup, "Self-reconstruction of a distorted nondiffracting beam," *Opt. Commun.* **151**(4-6), 207–211 (1998).
15. P. Martelli, M. Tacca, A. Gatto, G. Moneta, and M. Martinelli, "Gouy phase shift in nondiffracting Bessel beams," *Opt. Express* **18**(7), 7108–7120 (2010).
16. S. Chávez-Cerda, "A new approach to Bessel beams," *J. Mod. Opt.* **46**, 923–930 (1999).
17. K. Reivelt and P. Saari, "Bessel-Gauss pulse as an appropriate mathematical model for optically realizable localized waves," *Opt. Lett.* **29**(11), 1176–1178 (2004).
18. K. Reivelt and P. Saari, "Experimental demonstration of realizability of optical focus wave modes," *Phys. Rev. E Stat. Nonlin. Soft Matter Phys.* **66**(5), 056611 (2002).
19. G. Scott, "Efficient generation of nearly diffraction-free beams using an axicon," *Opt. Eng.* **31**(12), 2640–2646 (1992).
20. J. H. McLeod, "The axicon: A new type of optical element," *J. Opt. Soc. Am.* **44**(8), 592–597 (1954).
21. J. Turunen, A. Vasara, and A. T. Friberg, "Holographic generation of diffraction-free beams," *Appl. Opt.* **27**(19), 3959–3962 (1988).
22. J. Durmin, J. J. Miceli, Jr., and J. H. Eberly, "Comparison of Bessel and Gaussian beams," *Opt. Lett.* **13**(2), 79–80 (1988).

23. P. L. Overfelt and C. S. Kenney, "Comparison of the propagation characteristics of Bessel, Bessel-Gauss, and Gaussian beams diffracted by a circular aperture," *J. Opt. Soc. Am. A* **8**(5), 732–745 (1991).
24. R. M. Herman and T. A. Wiggins, "Bessel-like beams modulated by arbitrary radial functions," *J. Opt. Soc. Am. A* **17**(6), 1021–1032 (2000).
25. R. M. Herman and T. A. Wiggins, "Apodization of diffractionless beams," *Appl. Opt.* **31**(28), 5913–5915 (1992).
26. F. Gori, G. Guattari, and C. Padovani, "Bessel-Gauss beams," *Opt. Commun.* **64**(6), 491–495 (1987).
27. J. Arlt and M. J. Padgett, "Generation of a beam with a dark focus surrounded by regions of higher intensity: the optical bottle beam," *Opt. Lett.* **25**(4), 191–193 (2000).
28. P. Saari and K. Reivelt, "Evidence of X-shaped propagation-invariant localized light waves," *Phys. Rev. Lett.* **79**(21), 4135–4138 (1997).
29. R. Grunwald, U. Griebner, U. Neumann, A. Kummrow, E. T. J. Nibbering, M. Piché, G. Rousseau, M. Fortin, and V. Kebbel, "Generation of ultrashort-pulse nondiffracting beams and X-waves with thin-film axicons," in: M. Murnane, N. F. Scherer, and A. M. Weiner (Eds.), *Ultrafast Phenomena XIII* (Springer-Verlag, New York, 2002) 247–249.
30. R. Grunwald, V. Kebbel, U. Griebner, U. Neumann, A. Kummrow, M. Rini, E. T. J. Nibbering, M. Piché, G. Rousseau, and M. Fortin, "Generation and characterization of spatially and temporally localized few-cycle optical wavepackets," *Phys. Rev. A* **67**(6), 063820 (2003).
31. J. Y. Lu and J. F. Greenleaf, "Nondiffracting X waves. Exact solutions to free space scalar wave equation and their finite aperture realizations," *IEEE Trans. Ultrason. Ferroelectr. Freq. Control* **39**(1), 19–31 (1992).
32. J. Y. Lu and J. F. Greenleaf, "Experimental verification of nondiffracting X waves," *IEEE Trans. Ultrason. Ferroelectr. Freq. Control* **39**(3), 441–446 (1992).
33. M. Zamboni-Rached, E. Recami, and H. E. Hernández-Figueroa, "New localized Superluminal solutions to the wave equations with finite total energies and arbitrary frequencies," *Eur. Phys. J. D* **21**(2), 217–228 (2002).
34. M. Zamboni-Rached, E. Recami, and H. E. Hernández-Figueroa, "Theory of 'frozen waves': modeling the shape of stationary wave fields," *J. Opt. Soc. Am. A* **22**, 2465–2475 (2005).
35. M. Z. Rached and E. Recami, "Subluminal wave bullets: Exact localized subluminal solutions to the wave equations," *Phys. Rev. A* **77**(3), 033824 (2008).
36. M. Zamboni-Rached, "Unidirectional decomposition method for obtaining exact localized wave solutions totally free of backward components," *Phys. Rev. A* **79**(1), 013816 (2009).
37. A. Chong, W. H. Renninger, D. N. Christodoulides, and F. W. Wise, "Airy-Bessel wave packets as versatile linear light bullets," *Nat. Photonics* **4**(2), 103–106 (2010).
38. D. Abdollahpour, S. Suntsov, D. G. Papazoglou, and S. Tzortzakis, "Spatiotemporal Airy light bullets in the linear and nonlinear regimes," *Phys. Rev. Lett.* **105**(25), 253901 (2010).
39. R. Grunwald, M. Bock, V. Kebbel, S. Huferath, U. Neumann, G. Steinmeyer, G. Stibenz, J.-L. Néron, and M. Piché, "Ultrashort-pulsed truncated polychromatic Bessel-Gauss beams," *Opt. Express* **16**(2), 1077–1089 (2008).
40. R. Grunwald, *Thin-film microoptics - new frontiers of spatio-temporal beam shaping* (Elsevier, Amsterdam, 2007).
41. M. Bock, S. K. Das, and R. Grunwald, "Programmable ultrashort-pulsed flying images," *Opt. Express* **17**(9), 7465–7478 (2009).
42. P. Sprangle and B. Hafizi, "Comment on nondiffracting beams," *Phys. Rev. Lett.* **66**(6), 837 (1991).
43. J. Durmin, J. J. Miceli, Jr., and J. H. Eberly, "Durmin, Miceli, and Eberly Reply," *Phys. Rev. Lett.* **66**(6), 838 (1991).
44. M. Mansuripur, "The uncertainty principle in classical optics," *Opt. & Photon. News*, Jan. 2002, 44–48 (2002).
45. M. J. Bastiaans, "Uncertainty principle and informational entropy for partially coherent light," *J. Opt. Soc. Am. A* **3**(8), 1243–1246 (1986).
46. P. Saari and K. Reivelt, "Evidence of X-shaped propagation-invariant localized light waves," *Phys. Rev. Lett.* **79**(21), 4135–4138 (1997).
47. A. Siegman, "New developments in laser resonators," *Proc. SPIE* **1224**, 2–14 (1990).
48. R. Borghi and M. Santarsiero, "M² factor of Bessel-Gauss beams," *Opt. Lett.* **22**(5), 262–264 (1997).
49. R. M. Herman and T. A. Wiggins, "Rayleigh range and the M² factor for Bessel-Gauss beams," *Appl. Opt.* **37**(16), 3398–3400 (1998).
50. S.-A. Amarande, "Beam propagation factor and the kurtosis parameter of flattened Gaussian beams," *Opt. Commun.* **129**, 311–317 (1996).
51. R. Grunwald and M. Bock, "Spatio-spectral analysis and encoding of ultrashort pulses with higher-order statistical moments," in *Conference on Lasers and Electro-Optics/Quantum Electronics and Laser Science Conference and Photonic Applications Systems Technologies*, OSA Technical Digest Series (CD) (Optical Society of America, 2007), paper CThM2.
52. M. Bock, S. K. Das, and R. Grunwald, "Adaptive shaping of complex pulsed nondiffracting light fields," *Proc. SPIE* **7716**, 7950–7958 (2011).
53. Z. Mei and D. Zhao, "Controllable dark-hollow beams and their propagation characteristics," *J. Opt. Soc. Am. A* **22**(9), 1898–1902 (2005).
54. G. Rousseau, N. McCarthy, and M. Piché, "Description of pulse propagation in a dispersive medium by use of a pulse quality factor," *Opt. Lett.* **27**(18), 1649–1651 (2002).
55. M. Piché and R. Grunwald, private communication. In the discussion, the product of M² and P² was considered to be used to describe the spatio-temporal beam properties of pulsed Bessel beams.
56. B. Salik, J. Rosen, and A. Yariv, "Nondiffracting images under coherent illumination," *Opt. Lett.* **20**(17), 1743–1745 (1995).

57. R. Grunwald, S. Huferath, M. Bock, U. Neumann, and S. Langer, "Angular tolerance of Shack-Hartmann wavefront sensors with microaxicons," *Opt. Lett.* **32**(11), 1533–1535 (2007).
58. R. Grunwald, U. Neumann, U. Griebner, K. Reimann, G. Steinmeyer, and V. Kebbel, "Ultrashort-pulse wavefront autocorrelation," *Opt. Lett.* **28**(23), 2399–2401 (2003).
59. M. Bock, S. K. Das, C. Fischer, M. Diehl, P. Börner, and R. Grunwald, "Reconfigurable wavefront sensor for ultrashort pulses," *Opt. Lett.* **37**(7), 1154–1156 (2012).
60. R. Grunwald and M. Bock, "Spatially encoded localized wavepackets for ultrafast optical data transfer," JEOS:RP (submitted to).
61. M. Bock, S. K. Das, R. Grunwald, S. Osten, P. Staudt, and G. Stibenz, "Spectral and temporal response of liquid-crystal-on-silicon spatial light modulators," *Appl. Phys. Lett.* **92**(15), 151105 (2008).
62. I. Golub, "Fresnel axicon," *Opt. Lett.* **31**(12), 1890–1892 (2006).
63. R. Grunwald and M. Bock, "Programmable microoptics for ultrashort pulses," *Proc. SPIE* **7716**, 77160P, 77160P-8 (2010).
64. M. Bouafia, A. Bencheikh, L. Bouamama, and H. Weber, "M² quality factor as a key for mastering laser beam propagation," *Proc. SPIE* **5456**, 130–140 (2004).
65. R. Grunwald and M. Bock, "Programmable micro-optics for ultrashort pulses," *SPIE Newsroom* (2010).
<http://spie.org/x39625.xml?highlight=x2422&ArticleID=x39625>.

1. Introduction

The confinement of light in space and time is a fundamental challenge in physics [1–3] with various practical implications, e.g. for high-resolution microscopy, manipulation and acceleration of particles or cells, precision metrology, or nanostructuring. In recent experiments, for example, the spatial compression of femtosecond laser pulses down to the diffraction limit was demonstrated [4]. This limit can be broken with methods which typically take advantage of evanescent fields, plasmons, nonlinear processes or singular optics (*superresolution*). Another objective, however, is the localization of free propagating optical fields in the angular domain (*supercollimation*). Perfect supercollimation would mean that a wavepacket of finite diameter would propagate without any spread in transversal direction so that it behaves quasi particle-like. In nonlinear optics, this is approximated in media by steady-state self-trapping (needle solitons) [5]. Self-induced spectral reshaping via conical refraction [6–8] leads to the formation of light bullets of characteristic X-shape in space and time coordinates (nonlinear X-pulses). Furthermore, supercollimation was achieved in nano-engineered materials with anomalous photonic properties [9].

Theoretical approaches for linear localized wave phenomena (also referred to as "undistorted progressive waves" [10], "nondiffracting beams" [11], "diffraction-free beams" [12], etc.) are known for many decades as special solutions of wave equations for light or matter waves (for an overview, compare [13] and references cited there). Ideal Bessel beams were described as propagation-invariant solutions of the Helmholtz equation for conical waves [11,12] with infinite extension, radial field profiles governed by Bessel functions, non-zero axial field vectors, self-reconstruction properties [14], accumulating Gouy phase [15] and (depending on the parameters) subluminal, luminal or even superluminal group velocities (not related to any violation of the relativistic limitations of velocity). Because of the infinite generating fields, theoretical Bessel beams carry infinite total energy and are physically irrelevant. An alternative theoretical approach on the basis of superimposed Hankel functions [16] delivers Bessel beams of finite transversal extension. Physical approximations corresponding to finite energies can be obtained experimentally with optical systems transforming the input field into a wave with a conical angular distribution [17,18], e.g. by diffractive, refractive or reflective axicons [19,20] or holographic components [21]. Axicons [20] enable to generate finite, but (in comparison to focused Gaussian beams) significantly more extended focal zones [22]. The field profile of the perfect theoretical Bessel beams oscillates in all spatial directions including a vector component parallel to the propagation axis. In the simplest case, this spatio-temporal field can be described by the expression

$$U(r,t) = \exp[-i(kx - \omega t)] \cdot J_0(kr), \quad (1)$$

(J_0 = first-kind zero-order Bessel function, k = wave vector, ω = frequency, r = radial coordinate, t = time). The propagation characteristics of Bessel-like beams results from a transversal-to-axial transform by the conical beam structure and therefore can be modified by

apertures or radial beam profiles [23–25]. An important example are Bessel-Gaussian beams which result from Gaussian beam illumination [17,26]. Higher order Bessel beams with central intensity minima are obtained by transforming Laguerre-Gaussian beams with axicons [27]. The constructive interference of spectral field components of broadband, ultrashort-pulsed Bessel-like beams leads to linear X-pulses [28–30] which were known in acoustics from optimizing the operation of ultrasound transducers [31,32]. Superluminal as well as luminal localized pulses (“light bullets”) as solutions of the wave equations were previously predicted by theoretical works [33–36]. It was shown that “frozen waves” with spatial localization can be generated by a continuous superposition of waves and that arbitrary shapes like spikes, donuts or cylindrical surfaces can be obtained. By breaking the radial symmetry, other types of localized waves can be generated. Airy beams with asymmetric fringe distributions and distinctly curved propagation paths were formed linearly and nonlinearly. This type of wavepackets was also referred to as “light bullets” [37,38]. The degree of localization in Bessel, Bessel-Gauss, and Airy beams, however, is limited to a certain extent because of the energy contained in the wings of radially oscillating profile functions. The more the propagation path is curved, the higher is the number of sideband oscillation peaks.

In recent experiments with reflective axicons we demonstrated that fringe-free, high-aspect-ratio Bessel-like distributions (“needle beams”) can be formed. Non-oscillating profiles require a self-apodized truncation with apertures matched to a central maximum [39,40]. In this case, the energy of outer wings is lost (or one has to recycle it by coherent addition in a resonator structure). It was demonstrated that femtosecond needle beams also show a self-reconstruction phenomenon like pulsed Bessel beams [13,40]. An alternative, aperture-less method to realize the concept of needle beams is to reduce the axicon angle until the radius of the nondiffracting zone exactly matches the central lobe of the resulting Bessel distribution (supposed that magnetic field effects can be neglected). Both arrangements can be coupled with lenses or telescopes to further reduce or enhance the beam diameter. Reconfigurable axicon arrays were programmed in the phase map of a spatial light modulator (SLM) [40,41]. For sub-20-fs pulses, the spectro-temporal profiles of needle beams were found to propagate nearly unchanged whereas they are corrupted in outer fringes of Bessel beams and extended focal zones of Gaussian beams [39]. This better temporal stability compared to the foci of polychromatic Gaussian beams has to be emphasized as a specific advantage of needle beams and might be of importance for future ultrafast optical applications.

As we will show by experimental results with spatially programmable few-cycle pulses, such supercollimated, radially non-oscillating and temporally localized polychromatic beams are not restricted to needle beams. In this paper we propose to generalize these type of beams to a particular class of pulsed, “highly localized wavepackets” (HLW) which closely approximate perfect linear-optical light bullets. Spatio-temporal and angular free-space propagation properties for different types of HLW are demonstrated. Differences to other approaches of linear light bullets and potential applications will be discussed.

2. Spatial localization

The concept of nondiffracting beams was controversially discussed in comparison to Gaussian beams [42,43]. For a clear classification and a defined control of SLM-based systems for shaping localized beams, the spatial and temporal beam quality have to be quantitatively expressed by appropriate figures of merit. It is well known that the resolution of focusing systems is basically limited by an optical uncertainty relation between the widths in the spatial and spatial-frequency domain (positional and directional intensity [44,45]). Supercollimation can be approximated by subsequently generating focal spots at different positions along the optical axis. This can be achieved by the transversal-to-axial transformation by axicons. The interference of the superimposed coherent, conical partial waves results in the formation of Bessel-like waves or (at sufficiently large bandwidth) X-waves traveling along extended zones [46]. In general, the angular and spatial confinement of

3D-beams can roughly be described by the beam propagation factor M^2 [47] which is related to the radial and angular variances σ_o and σ_f in the near- and far-field, respectively:

$$M^2 = 4\pi\sigma_o\sigma_f \quad (2)$$

For Bessel-Gauss beams, analytical expressions for M^2 are known [48,49]. The application of these approximations, however, to the more general situation with adaptive compensation of input beam divergence, radially variable conical angles and axially variable beam quality is not simply possible and a comparable beam propagation factor can hardly be defined. Instead of that, radial and axial decay parameters can be used to define “beam waists” and “confocal parameters” in analogy to the Gaussian beam. For nonlinear applications or adaptive reshaping of beam profiles (e.g. off-axis arrangements or imaging through distorting media) where small variations of the intensity distribution are of particular importance, higher order statistical moments like kurtosis [50] and skewness [51,52] can be used as additional, compact measures for peakedness and symmetry. In the literature it was shown that dark hollow beams (DHBs) with central intensity minima can also be characterized by M^2 and kurtosis [53].

The special case of needle beam arrays that are generated by dividing the wavefront of an extended Gaussian beam with ultraflat phase axicons programmed into an SLM [39,40] is of particular relevance for applications (e.g. generation of “flying images” [41]). Self-apodization without truncation is obtained, if the geometrical parameters are chosen to generate exactly the central lobe of a Bessel distribution and no outer fringes. In this configuration, the parts of the wave illuminating the segments can be regarded, in good approximation, to be plane waves. The foot-to-foot-diameter D of a monochromatic needle beam at an axial position z depends on the wavelength λ and the conical angle θ (half angle against the optical axis):

$$D(z) = f(z) \frac{\lambda}{2n \sin \theta} \quad (3)$$

(n = refractive index of air). For polychromatic beams with sufficiently narrow or symmetric spectral profiles, λ can be replaced by the center-of-gravity wavelength λ_0 . The scaling factor f mainly depends on the divergence of the illuminating beam. Further modifications arise from the diffraction at the edges of the programmed axicons. At small conical angles, the vanishing “contact angle” at the rim leads to a phase apodization which reduces the diffraction. The decay of intensity in the SLM plane along the radius r results from the coherent superposition (spectral interference) of all conical contributions. In the center of the zone of constructive interference at the distance z_0 , it is proportional to the square of the first-kind, zero-order Bessel function $J_0^2(r)$ within the limits of the first zero (first dark ring):

$$I_{NB}(r) \propto f(z_0) \cdot J_0^2 \quad \text{for } r < r_1 \quad (4a)$$

$$I_{NB}(r) = 0 \quad \text{for } r > r_1 \quad (4b)$$

(r_1 = radius of the first minimum of J_0^2). The axial extension of the nondiffracting propagation zone (“confocal parameter”) can be defined by two characteristic distances z_1 and z_2 where, in analogy to the Gaussian beam description, the beam area is doubled and the intensity at the axis is reduced by a factor of 2 (FWHM extension). A more comprehensive theoretical description of the beam quality of localized beams (e.g. by means of the Wigner function) would have to take into account that inside the zone of constructive interference, each point in space is the origin of a bundle of rays (corresponding to a local wavefront ambiguity).

3. Spatio-temporal localization

In analogy to the spatial beam quality, the temporal shape of ultrashort pulses can formally be described by a pulse propagation factor P^2 [54]:

$$P^2 = 4\pi\sigma_v\sigma_t \quad (5)$$

where σ_v and σ_t are the variances in spectral and temporal domain, respectively. Thus, a dimensionless *spatio-temporal localization parameter* L^2 of an ultrashort-pulsed wavepacket can be defined by the root of the product of M^2 and P^2 [55]:

$$L^2 = \sqrt{M^2 \cdot P^2} = 4\pi \cdot \sqrt{\sigma_0\sigma_f\sigma_v\sigma_t} \quad (6)$$

The quality parameters are spatially (M^2) and temporally integrated (P^2) so that this approximation is valid only in the paraxial case (small angles, negligible travel time effects). For non-paraxial propagation (large angles), L^2 cannot be applied because spatial and temporal features are not fully separable. In the most experiments reported here, the paraxial case was well approximated by working at extremely small conical angles and can serve as a figure of merit for the localization of wavepackets in space and time. It has to be noted, however, that the localization of HLW cannot completely be described by the used approach. Improved models require to include temporal changes of spatial and angular parameters (e.g. in frame of the Wigner function). For pulses with pulse durations beyond the area of validity of the slowly varying envelope approximation, however, the determination of the temporal and spectral statistical parameters requires a more sophisticated analysis.

4. The class of highly localized wavepackets (HLWs)

Pulsed needle beams (needle pulses) are localized both in space and in time. As mentioned, the main difference to other linear light bullets like pulsed Bessel beams is to appear without any radial oscillations of the intensity distribution. This makes them, finally, to the true candidates for real linear light bullets (in particular for the case of single cycle pulses where both the spatial and the temporal profiles exhibit only single maxima of the optical field).

We will show that the characteristic properties of ultrashort-pulsed needle beams addressed here can also be realized in further types of quasi-nondiffracting wavepackets. By particularly breaking the symmetry of radially symmetric needle beams but preserving their key propagation properties, the case of needle beams can be generalized to a class of radially non-oscillating wavepackets with spatially and temporally undistorted propagation over extended ranges we refer to as “highly localized wavepackets” (HLWs). The basic idea of combining diffraction-free spatial filtering with certain geometrical transforms is illustrated in Fig. 1.

The intensity profiles of HLWs are related to extremum properties. Similar to transform-limited pulses in temporal Fourier transform, the spatial frequency spectrum of HLWs is coupled with a minimum diffraction because of apodization. The experimental realization of such HLWs is enabled by the capability of spatial light modulators to flexibly tailor arbitrary angular distributions of phase elements in extremely narrow angular intervals. The HLWs of most simple structure (“elementary HLWs”) can be used as building blocks for composing complex patterns [52]. Contrary to alternative approaches based on enhancing the depth of focus of complete, monochromatic, coherent images by optimizing the diffraction with adapted amplitude-phase-masks [56], the image information is encoded in an finite number of channels which keep separated over an extended (nondiffracting) zone. Because of their high aspect ratios, self-reconstructing behavior [13] and tilt tolerance [57], needle beams were recently applied to spatially resolved autocorrelation [58], reconfigurable wavefront sensing [59] and high-speed optical data transfer [60] with Ti:sapphire laser pulses in 10-20-fs range.

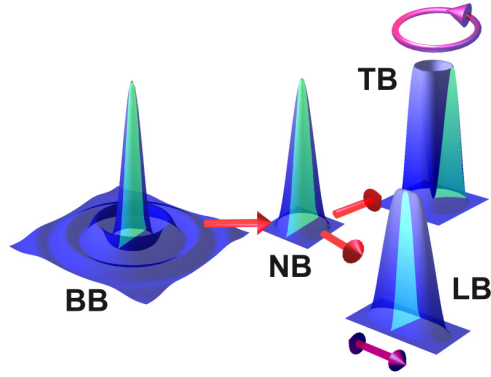


Fig. 1. Principle of generating highly localized wavepackets (HLWs). Self-apodized (diffraction-free) spatial filtering of a pulsed Bessel beam (BB) is used to generate a radially symmetric needle beam (NB). By linear and circular transform algorithms (circular and double arrow), non-radially symmetric profiles of stretched (linear beam, LB) and tubular structure (tubular beam, TB) can be obtained. The propagation remains quasi-nondiffracting in the spatial and temporal domain.

In the following sections, the experimental realization of HLWs with programmable generalized axicons at pulse durations down to the sub-3-cycle range (6 fs) is reported. Spatial and temporal localization and pulse transfer properties of HLWs with needle-shaped, tubular and linear intensity maps are discussed. The idea to synthesize quasi-continuous complex nondiffracting images by fusing such dissimilarly shaped “elementary” HLWs is considered.

5. Experimental realization of HLWs

5.1. Experimental techniques

Figure 2 shows the experimental setup consisting of a pulsed light source (Ti:sapphire laser oscillator VENTEON PULSE: ONE PE, minimum pulse duration 6 fs, center wavelength 800 nm, FWHM spectral bandwidth 300 nm, pulse energy up to 7 nJ, repetition frequency 80 MHz), an interferometer, an active beam shaper and (depending on the measuring task) adapted detection systems.

Initial pulse duration and spectral phase were performed with a second-harmonic autocorrelator (Mini, APE) and an FC-SPIDER (few-cycle spectral phase interferometry for direct electric field reconstruction) (APE) (not drawn in the schematic representation). For a flexible shaping of HLWs, different types of low-dispersion LCoS-SLMs were used depending on the requirements (maximum phase step, resolution, fill factor). All devices worked in reflection (liquid crystal layer on mirror) with either a parallel or vertical alignment and a layer thickness between 3 and 18 μm . Maximum phase differences up to $> 4\pi$ at a wavelength of 800 nm could be obtained. To approximate HLWs with quasi-nondiffracting propagation characteristics, single and multiple conical phase elements (axicons) and related structures (generalized axicons) were programmed into the phase map of the LCoS-SLM under test. This was possible on the basis of known calibration curves for the spectral phase depending on the gray values of the graphic processor software of the SLM [61]. In these previous experiments it was found that Gires-Tournois interference is responsible for slight periodical spectral-dependent phase distortions can be minimized by a proper choice of the SLM parameters. For example, the corresponding pulse lengthening without re-compression was in the range of 2 fs for input pulses of 15 fs (4 μm LC layer).

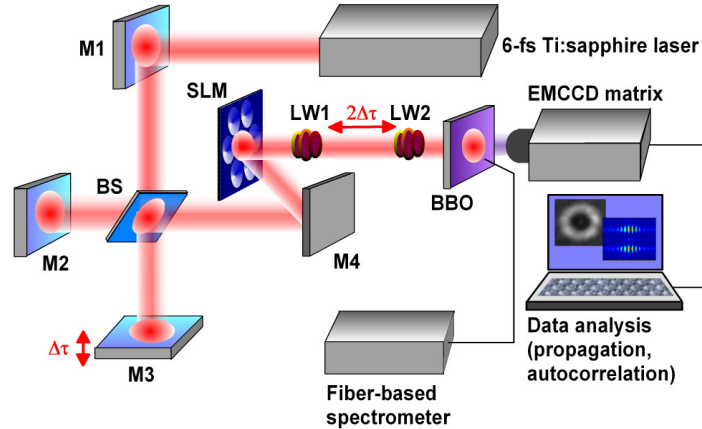


Fig. 2. Setup for the generation and characterization of programmable HLWs (schematically). The pulses emitted by a Ti:sapphire oscillator (Venteon, minimum pulse duration 6 fs, center wavelength 800 nm, FWHM spectral bandwidth 300 nm, pulse energy 7 nJ, repetition frequency 80 MHz) are shaped with an LCoS-SLM. The time-integrated intensity distribution is detected with a CCD or EMCCD camera (EMCCD). For a 2D spatially resolved analysis of the temporal pulse properties, second order autocorrelation is performed with a balanced interferometer (M1-M4 = mirrors, BS = beam splitter, BBO = beta barium borate crystal for SHG) by tuning the length one interferometer arm. The resulting time delay $\Delta\tau$ is doubled in a round trip and leads to a final delay of $2\Delta\tau$ between the pulse replicas. Spectral maps are detected with a position-controlled fiber spectrometer (Ocean optics).

Beside approximately cone-shaped phase profiles (Fig. 3(a)), Fresnel-axicons (“fraxicons” [62]) consisting of concentric rings similar to zone lenses, torus-shaped axicons (Fig. 3(b)) [52], elliptical axicons, linearly-conical axicons (Fig. 3(c)), bi-microprisms and combinations of such elements were used to generate different types of HLWs. The time-integrated spatial intensity profile was detected with a CCD (not drawn) or a cooled EMCCD camera (drawn). The highly sensitive EMCCD detection was necessary in case of very weak signals, e.g. from 2D second harmonic generation (SHG) excited by the few-nJ pulses. For a spatially resolved temporal pulse analysis, collinear autocorrelation was measured by tuning the arm length of a Michelson interferometer (formed by the of mirrors M1, M2 and M3 and a symmetric broadband beam splitter BS). Additionally, 2D spectral maps were detected with a fiber-based spectrometer (Ocean optics) on a three-axis translation stage. The second order autocorrelation function was obtained by analyzing the SHG signal generated in a thin beta-barium borate (BBO) crystal. In few-cycle experiments with pulse durations < 10 fs at the input of the SLM, the dispersion of the optical components was pre-compensated by a pair of chirped mirrors.

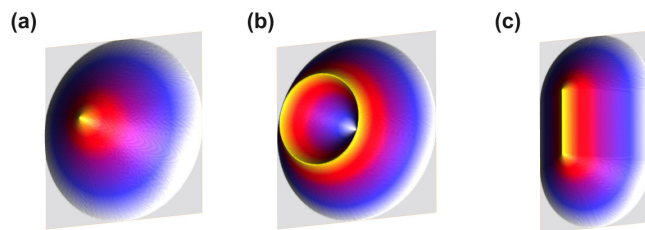


Fig. 3. Selected basic types of axicons for the generation of highly localized wavepackets: (a) conus axicon shaping needle beams, (b) torus axicon shaping tubular beams, and (c) stretched conus axicon with central bi-prismatic zone shaping linear beams (effective height profiles, schematically). Possible apodization (e.g. by flattened contact angles) is not shown here.

It has to be mentioned that the spectral dispersion can be a limiting factor for angular shaping at large spectral bandwidth. Because of the very small applied angles, however, in particular in the generation of needle beams and other highly localized wavepackets, the overlap zone of the spectral compartments remains much larger compared to the distorted zone and the effect can be neglected in good approximation in our case.

5.2. Few-cycle pulsed needle beams

Uniform and non-uniform arrays of ultrashort-pulsed needle beams with spatial periods between $p = 80 \mu\text{m}$ and $p = 500 \mu\text{m}$ and different geometrical arrangements (hexagonal, rectangular) were programmed in different types of LCoS-SLMs (HoloEye) with maximum phase steps between π and 2π at the center wavelength of 800 nm [63]. The pixel size was in all cases about $8 \mu\text{m}$. At short pulse durations in few-cycle range, the corresponding axial extension of the individual wavepackets (few micrometers) was typically three orders of magnitude smaller than the radial dimensions of the arrays (few millimeters). In fact, ultraflat wavepackets with a low number of field oscillations (similar to a stack of pancakes) propagate through a needle-shaped zone of low distortion (nondiffracting zone). To minimize unwanted dispersion, the LCoS-SLMs were operated without beam splitters in oblique incidence at incident angles of up to 50° . The resulting aberrations (ellipticity) were adaptively corrected as it was recently demonstrated in the frame of reconfigurable Shack-Hartmann wavefront applications and two-dimensional temporal mapping with pulsed needle beams [59]. If the self-apodizing condition [39–41] is fulfilled, the angular diameter of a needle beam is determined by the conical angle after passing the axicon, the center wavelength and the divergence of the illuminating beam. In Fig. 4, the propagation of pulsed diffractive and nondiffractive twin beams generated from the Ti:sapphire oscillator beam are compared to each other. In the starting plane, a hard circular aperture (Fig. 4(a), left) and an ultraflat axicon (Fig. 4(a), right, conical angle 0.13°) were programmed into the SLM phase map via gray values. Both elements had the same radius of $380 \mu\text{m}$. The resulting time-integrated intensity profiles were detected at distances of $z_1 = 18.5 \text{ mm}$ and $z_2 = 138.5 \text{ mm}$ (Figs. 4(b) and 4(c), respectively). The double beam structure enables to quantitatively evaluate specific multi-beam effects like cross-talk and interference.

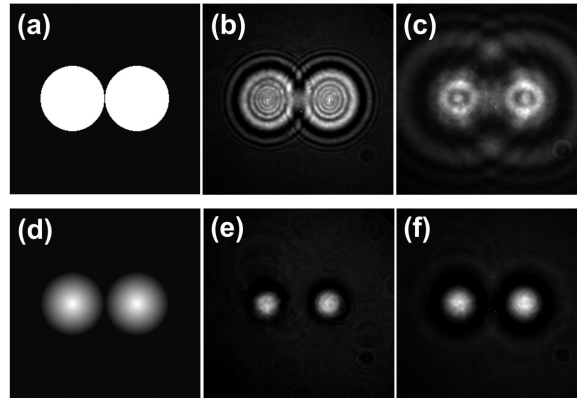


Fig. 4. Comparison of the propagation characteristics of pulsed diffractive and nondiffractive twin beams, left: phase distributions of pairs of (a) hard circular apertures and (d) flat axicons programmed into the SLM as gray value maps. The maximum brightness in (a) indicates the largest phase value for this device (π). Pictures (b),(e) and (c),(f) show intensity profiles measured at distances of $z_1 = 18.5 \text{ mm}$ and $z_2 = 138.5 \text{ mm}$, respectively. Double beams were chosen to study cross-talk and interference effects of neighboring beams (radii: $380 \mu\text{m}$; average conical angle of axicon: 0.13° , incident angle about 20°). The field of view was $2.3 \times 2.3 \text{ mm}^2$ in all cases.

Figures 5(a) and 5(b) show the radii (defined by the transversal decay down to $1/e^2$ of the maximum intensity) and the intensity as a function of the propagation distance in a simulation

for a monochromatic Gaussian beam (red, circles) in comparison to experimental data for a polychromatic 6-fs pulsed needle beam (blue, squares). The green dashed line in Fig. 5(b) is related to the input intensity at the center of the cross section of the illuminating Gaussian beam. Between $z = 60$ and $z = 100$ mm, a focus zone with > 4 -times enhanced intensity appears. If an equivalent parameter z_N corresponding to a Rayleigh length is calculated, it is not surprising that one obtains inconsistent values on the basis of expanding radius and decaying intensity (110 and 150 mm, respectively). A Gaussian beam of comparable initial geometry behaves significantly different ($z_G = 85$ mm) so that we find a strong indication for a quasi-nondiffracting propagation of the adaptively generated wavepackets.

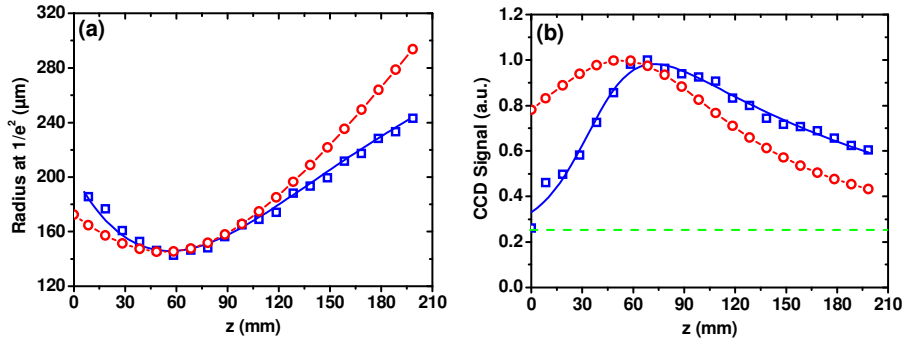


Fig. 5. Comparison of the propagation of Gaussian and needle beams (data corresponding to Figs. 4(e,f)): (a) increase of the radii (radial intensity decay to $1/e^2$) as a function of distance; circles: simulation for monochromatic (800 nm) Gaussian beam; squares: experimental data for a polychromatic needle beam (Ti:sapphire oscillator, pulse duration 6 fs), (b) measured and theoretical center intensity as a function of distance for a needle and Gaussian beam, respectively (green dashed line: input intensity without phase profile at zero voltage). The lines represent fit curves. To enable a better comparison, the Gaussian beam was transferred to the waist position of the needle beam. The deviations in the beginning of the propagation of the needle beam result from a non-perfect shape of the axicons in the central region.

These results indicate an excellent propagation behavior of the needle beams even at few-femtosecond pulse durations and correspondingly broad spectral bandwidths. For the quantitative characterization, the temporal aspect has to be carefully analyzed as well. In the case of arrays of beams, however, most of the established methods for pulse diagnostics (e.g. SPIDER or FROG) can hardly be applied. Therefore we used the nonlinear two-dimensional autocorrelation (combining an interferometer with an EMCCD detector) to diagnose the pulses with spatial resolution and high conversion efficiency [59]. Figure 6 shows the spatially resolved temporal structure of multiple needle beams reconstructed from two-dimensional second-order autocorrelation.

The matrix of generating axicons was programmed into the phase-map of an SLM (period 720 μm , phase modulation depth 400 nm, conical angle 0.13°) which was illuminated by a 6.5-fs Ti:sapphire oscillator pulse (incident angle 43°). A 10 μm thick BBO crystal was used as frequency converter. For a better visualization, the time-dependent electrical field amplitude was modified by adding a fixed DC value and encoding size and brightness of the maxima according to the absolute value of the field. The radial beam waist radius w_0 at the chosen distance of $z = 100$ mm was found to be 150 μm . The distances of neighboring maxima indicate the cycles of the electric field (2.7 fs at 800 nm central wavelength).

The analysis of individual sub-beams in space and time enables to describe the localization of the wavepackets in a first approximation (i.e. within the frame of a simplified model as described in section 3). According to the formalism reported in [60], the value for the beam propagation factor M^2 was determined to be 1.8.

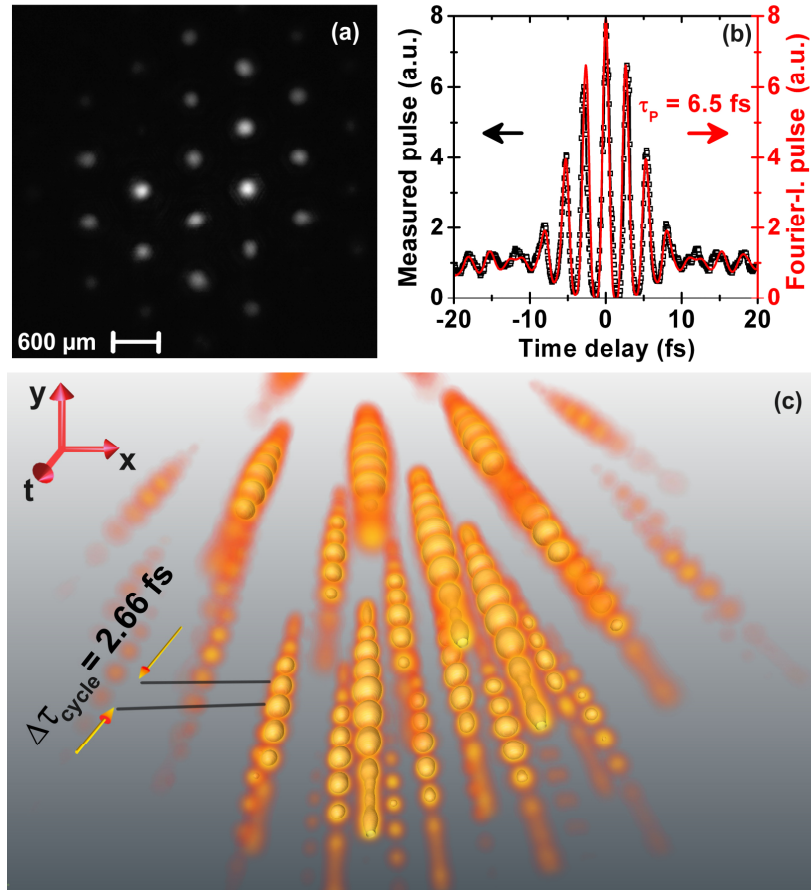


Fig. 6. Nonlinear characterization of multiple few-cycle wavepackets at a distance of 100 mm generated by an array of conical profiles (axicons) programmed in the phase map of an LCoS-SLM: (a) intensity distribution at zero time delay, (b) autocorrelation trace for a selected position in comparison to a theoretical bandwidth-limited pulse (flat spectral phase), (c) Visualization of the spatio-temporal structure by post-processed data of spatio-temporal 2nd order autocorrelation (fixed DC value added, size and brightness encoded according to the absolute value, perspective drawing with vanishing point). Conditions: axicon period 720 μm , effective height 400 nm, conical angle 0.13°, incident angle 43°; source: Ti:sapphire oscillator, nonlinear converter: 10 μm thick BBO crystal, pulse duration 6.5 fs, detector: EMCCD).

From the autocorrelation measurement, a pulse propagation factor of $P^2 = 1.75$ can be assumed. Both factors yield a spatio-temporal localization parameter according to Eq. (6) of $L^2 = 1.77$ related to the conditions of our experiment. To compare, a double-transform limited HLW of Gaussian shape in space and time would have a theoretical localization factor of 1. It has to be noted that the application of M^2 (as defined for Gaussian beams) to nondiffracting HLWs delivers a quantitative description but has to be treated with caution because of the ambiguity of the wavefront in the superposition zone. Modified localization parameters could consider a propagation dependence and differ between near and far field.

As already mentioned, needle beams can also be shaped by zone axicons (“fraxicons”). In the case of a monochromatic cw-source, the discrete profile can be optimized by implementing steps of exactly 2π at the transition between neighboring zones. For a polychromatic ultrashort-pulsed source, however, the axicons can only be perfectly adapted to a narrow wavelength interval. Moreover, the pulse travel time experiences a delay between adjacent zones. Therefore, the fidelity of pulse transfer with fraxicons depends stronger on the pulse duration and axicons with continuous phase profiles are more suitable.

Because of diffraction and scattering caused by substructures of the shapers (pixels, phase steps) and overlap of multiple beams, a non-negligible background signal is generated. This reduces the energy transfer efficiency significantly (depending on the system configuration). Further improvements of the contrast should be possible by spatial filtering.

5.3. Few-cycle nondiffracting light rings

Ultrashort-pulsed dark hollow beams were shaped by programming toroidal axicons in LCoS-SLMs [63]. The phase profiles of two selected elements as gray value maps and cut curves with effective heights can be found in Fig. 7. To classify toroidal axicons of different symmetry of their the ring profile, we define a symmetry factor SF as the ratio

$$SF = \frac{2r_i}{R} \quad (7)$$

where r_i and R are the inner radius (center-to-peak) and outer radius (center to rim) (see Fig. 7(c)). The symmetry factors were $SF = 0.50$ and 1.00 in Figs. 7(a), 7(b) and in the curves with red dots and blue squares in Fig. 7(c), respectively.

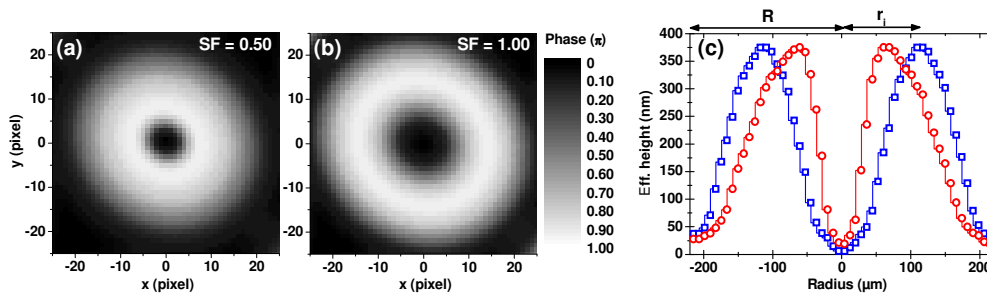


Fig. 7. Programmable torus axicons: comparison of two discretized structures of different symmetry. (a) and (b): 2D gray value maps (1 pixel), (c) linear cuts with effective height profiles. The corresponding symmetry factors were $SF = 0.50$ in the picture (a) and the curve with red dots in (c), and $SF = 1.00$ in (b) and the curve with blue squares in (c).

The steps in Fig. 7(c) result from discretized phase levels. Figure 8 demonstrates the propagation properties of the individual ring-shaped HLWs which were sub-beams of a hexagonal array (period about $430 \mu\text{m}$, Fig. 9). The profiles with blue squares, green circles and red triangles in Fig. 8(a) show central cuts through the intensity maps shaped at SF values of 0.5, 0.7 and 0.9, respectively. The best overall contrast was obtained at a distance of $z = 8 \text{ mm}$ whereas inner and outer contrast $C_i = 84\%$ and $C_a = 55\%$ were nearly constant for all values of SF . The hollow beam diameter (peak-to-peak distance for central cuts) depends, in good approximation, linearly on the SF (Fig. 8(b)). An intensity map of a part of the hexagonal beam array detected at a distance of 8 mm is shown in Fig. 9(b). A 3D-plot of the hollow beam array (see Fig. 9(a)) was reconstructed using all measured depth information. The period was about $430 \mu\text{m}$ after slightly correcting for elliptical distortion introduced by the deviation from normal angle of incidence (20°). The procedure was similar to the correction of aberrations described in a recent paper on adaptive wavefront sensing of ultrashort pulses with needle beams in a reflective setup [59].

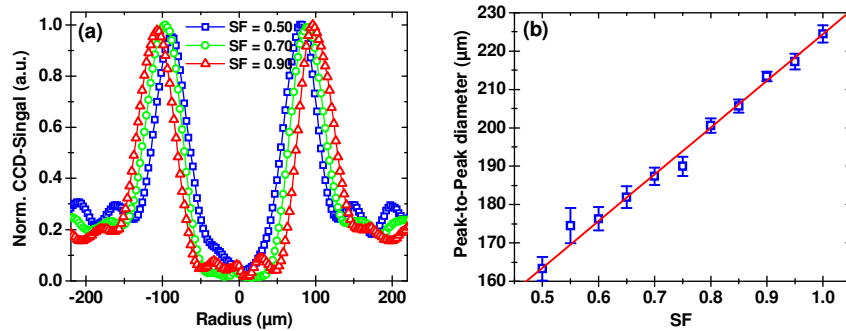


Fig. 8. Geometry of hollow beams as a function of the axicon symmetry: (a) intensity profile at a distance of $z = 8$ mm for $SF = 0.5$ (blue squares), 0.7 (green circles) and 0.9 (red triangles). At this distance, the best overall contrast was obtained. Inner and outer contrast $C_i = 84\%$ and $C_o = 55\%$ keep nearly constant over the considered range of SF ; (b) dependence of the hollow beam diameter (peak-to-peak distance for central cut) on SF . One recognizes that the diameter scales linearly with this parameter in a fairly good approximation.

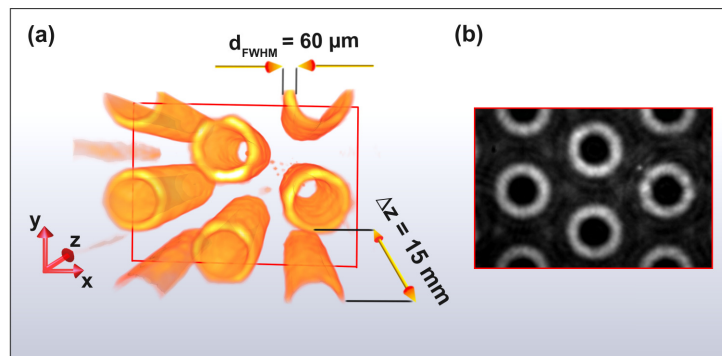


Fig. 9. Propagation of a hollow beam array (a) 3D-reconstruction from measured x -, y - and z -intensity data (b) Intensity map of a hexagonal array of hollow beams generated with an LCoS-SLM (period about $430 \mu\text{m}$, distance $z = 8$ mm, ellipticity corrected by a linear transform factor $SF = 0.9$ in one direction, field of view: $1.2 \times 0.8 \text{ mm}^2$).

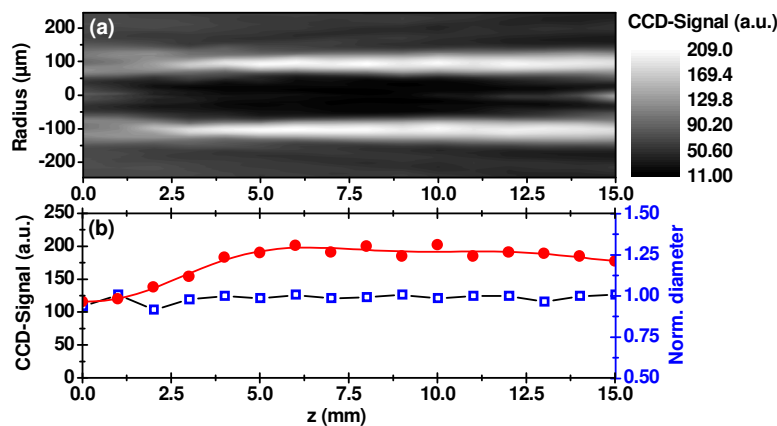


Fig. 10. Stable propagation zone of a pulsed hollow beam generated with an asymmetric toroidal axicon ($SF = 0.8$): (a) intensity profiles measured at distances between 0 and 15 mm; (b) peak intensity (red dots) and normalized diameter (related to a reference diameter of $394 \mu\text{m}$) as a function of distance (please notice the different scales for CCD-signal and diameter).

The propagation zone of a pulsed hollow beam generated with a torus-shaped axicon of a symmetry factor $SF = 0.8$ is shown in Fig. 10. Two-dimensional intensity maps were detected with a CCD camera for distances between 0 and 15 mm. The plot in Fig. 10(a) represents a central radial cut through the obtained image 3D data. Within the first few millimeters, the four separated light fields shaped by the torus profile start to overlap and to create an extended tubular zone of stable propagation. The contrast (peak-to-center) reaches values > 0.8 . Corresponding curves for peak intensity (red dots) and normalized diameter D/D_0 (related to a reference diameter of $D_0 = 394 \mu\text{m}$) are drawn in Fig. 10(b). It is evident that the radial extension of the hollow beam experiences no significant changes over the whole propagation distance. The temporal transfer was characterized by measuring the second order autocorrelation function. At a fixed axial distance the measured pulse duration was still 6.5 fs.

The propagation behavior was also studied for single hollow beams of 8-times larger diameter (Fig. 11). It was found that the FWHM of the autocorrelation function varies only slightly with the increasing distance (at a correspondingly larger Rayleigh length). The iso-field representation in Fig. 12 clearly indicates a few-cycle ring-shaped wavepacket (“ring bullet”) obtained by linear-optical shaping by broadband free-space conical beams.

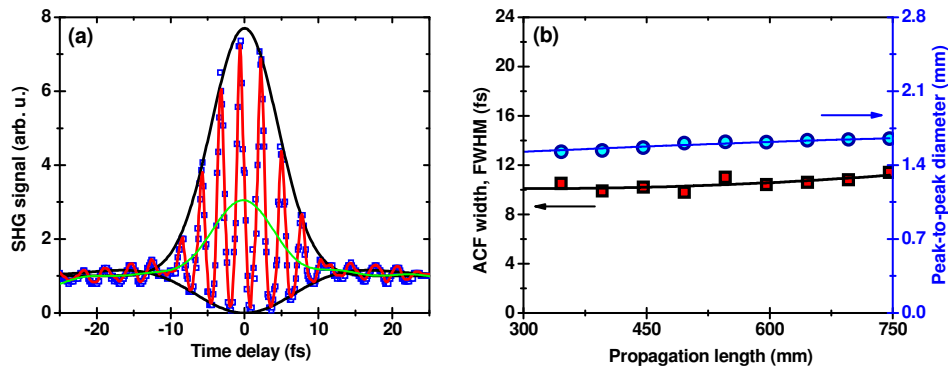


Fig. 11. Temporal properties of a solitary few-cycle ring-shaped HLW generated by programming a toroidal axicon (outer diameter 3.2 mm, conical beam angle 0.029°) into an LCoS-SLM: (a) 2nd order autocorrelation function (ACF) measured at a distance of 400 mm (FWHM 9.8 fs, green line: derived intensity autocorrelation), (b) propagation-dependent FWHM of the ACF (black squares) and peak-to-peak ring diameter (blue circles). The averaged pulse duration along the zone was 6.7 ± 0.2 fs.

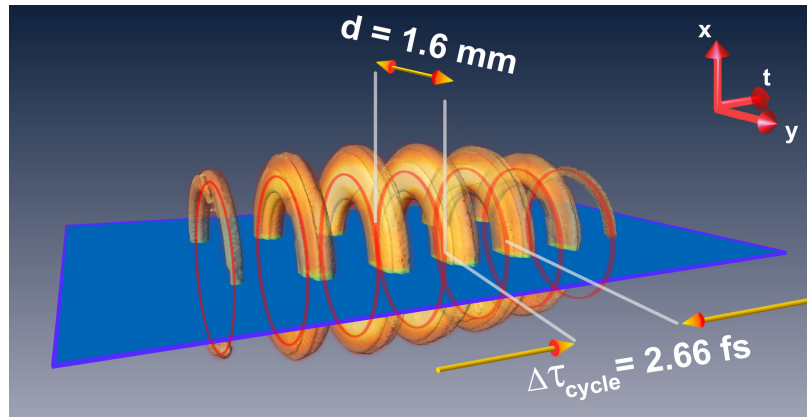


Fig. 12. Reconstructed time-dependent E-field of the HLW. To indicate the structure of a ring-shaped light bullet, the iso-electric-field surface of 6.8-fs pulses was retrieved from spatially resolved second-order autocorrelation. For visualization purposes, a DC-field (corresponding to the maximum field amplitude) was added [64] (red circles: field maxima, d = maximum-to-maximum ring diameter, $\Delta\tau_{\text{cycle}}$ = field oscillation period in time).

5.4. Few-cycle nondiffracting light blades and patterns composed of linear elements

To obtain radially stretched quasi-nondiffracting focal zones, ultraflat bi-prisms were programmed. A stack of nondiffracting pulsed light blades with a period of $200\ \mu\text{m}$ perpendicular to the optical axis is displayed in Fig. 13. Such light blades are of increasing interest for the spatially selective multiphoton fluorescence excitation of gases (e.g. for spectroscopy and turbulence analysis of flames in combustion engines) or biological matter (e.g. brain tissue). Other applications of linear nondiffracting focal zones are the high-speed depth-independent laser-machining of non-planar surfaces (e.g. 3D-texturing), transient poling of nonlinear materials, manipulation and acceleration of particles, and non-uniform plasmon excitation.

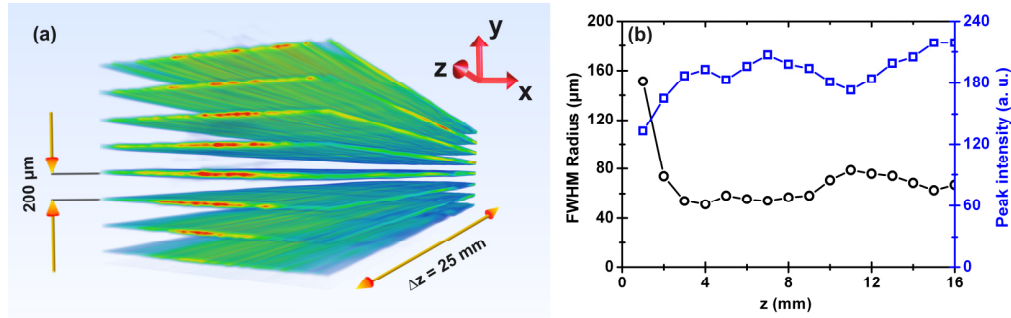


Fig. 13. Stack of pulsed nondiffracting linear HLWs (light blades) generated from the Ti:sapphire oscillator beam: (a) 3D plot with a nonlinear dependence of the color coded structure on the intensity (initial pulse duration 6.5 fs, perspective drawing with vanishing point, see Media 1); (b) axially dependent thickness of the light blades. Within the first 15 mm of propagation it was found to be about $60\ \mu\text{m}$.

Recently we demonstrated that linear elementary HLWs can also be applied to for the spatial encoding of few-cycle pulsed “flying images” [41,63]. As an example, the nearly undistorted propagation of a pattern (logo of MBI) is shown in Fig. 14. A selected feature of this image was analyzed more in detail. The intensity profile along a cut of $160\ \mu\text{m}$ through one partial line focus (Fig. 15(a)) was measured as a function of the propagation distance (Fig. 15(b)). The FWHM radius (Fig. 15(c)) shows a moderate increase and an aspect ratio (ratio of Rayleigh range: initial radius) of about 200:1. Image information can be extracted over a much more extended range by applying standard image processing procedures.

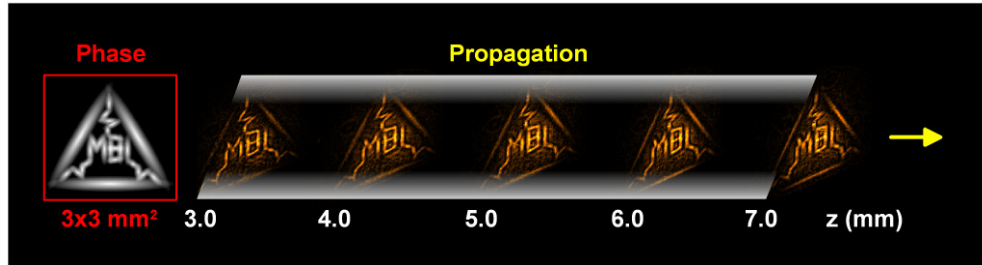


Fig. 14. Quasi-undistorted propagation of a small-scale ultrashort-pulsed pattern (MBI logo) composed of linear HLWs as elementary beams [52,65]. The “flying images” were generated by programming bi-prismatic microaxicon profiles in the phase map of an LCoS-SLM (red square, left). These experiments were performed with a Ti:sapphire laser oscillator at pulse duration of 13 fs and a center wavelength of 800 nm (image detection with CCD camera, image contrast slightly enhanced). A movie of the propagation is found in Media 2 for 13 fs (between $z = 2.5$ and 8.5 mm) and in Media 3 for 6.5 fs pulses (between $z = 0.0$ and 5.0 mm).

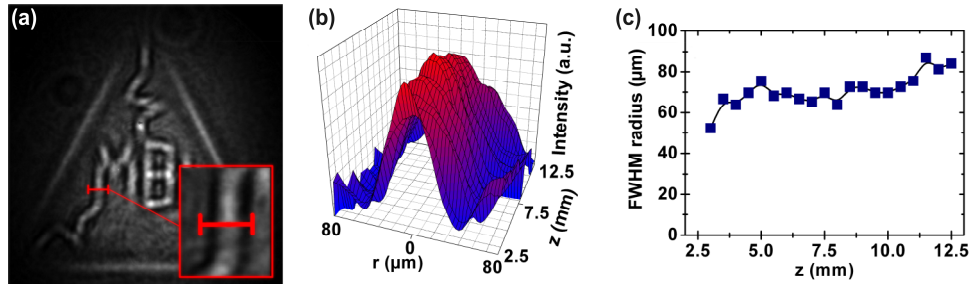


Fig. 15. Propagation dependent contrast of a selected feature (a) of the pattern corresponding to the experimental data used for Fig. 14 (red bar: cut, inset in red square: enlarged cut area). For distances < 10 mm, high contrast was observed (b). The increase of the FWHM diameter of the image feature as a function of the propagation distance is indicated in (c).

Quasi-nondiffracting ultrashort-pulsed patterns of even higher complexity can be composed by combining different types of elementary HLWs. The temporal transfer was not directly measured for the complex HLWs shown in this section. From measurements with needle and tubular beams with feature sizes in a comparable range (sub-100 μm field structures) we expect similar pulse durations.

6. Conclusions

The concept of pulsed needle beams as a particular approximation of spatio-temporally undistorted progressive waves can be generalized to a class of pulsed beams we refer to as “highly localized wavepackets” (HLWs). Mathematically, HLWs can be generated from needle beams by applying simple geometrical transforms (linear stretching and/or rotation). This leads to modified symmetry properties at, at the same time, persistently small spatial and temporal distortions at pulse durations down to a few femtoseconds. In previous experiments, “flying images” were composed of addressable needle beams of identical shape. In contrast to this, HLWs of circular, elliptical, linear or ring shape can serve as building blocks (“elementary” HLWs) of even more complex, segmented nondiffracting images encoded in ultrashort-pulsed light fields. The freedom of programming enables for generating arbitrary shapes. In experiments at pulse durations of down to 6 fs, needle beams, tubular beams (dark hollow beams) and linear beams (light blades) of flexible parameters were obtained by programming circular, toroidal and bi-prismatic shaped axicons in the phase map of an LCoS-SLM. Aberrations caused by working at oblique angles are corrected by an adapted off-axis design. It should be emphasized that the generated needle-type HLWs can be regarded as linear-optical “light bullets” which do not require any nonlinear effects to compensate the diffraction over significantly extended depth of focus.

For quasi-nondiffracting light fields at pulse durations where approximations like slowly varying envelope approximation and narrow bandwidth models break down [2] it is expected that the limits of localization have to be redefined and standardized quantitative measures like the beam propagation factor have to be replaced by more adequate parameters in future.

Acknowledgments

The authors thank T. Elsaesser and G. Steinmeyer (MBI), A. Friberg (University Helsinki), P. Saari (University Tartu), H. Weber (Technical University Berlin) and M. Piché (Laval University Quebec) for stimulating discussions. We gratefully acknowledge the collaboration with HoloEye AG (Berlin), APE GmbH and metrolux GmbH (Göttingen). The work was supported in part by German Research Foundation (project no. GR 1782/7-1).